



# Inverse heat transfer technique for estimation of focal flux distribution for a concentrating photovoltaic (CPV) square solar parabola dish collector



N. Premjit Singh<sup>\*</sup>, K.S. Reddy<sup>\*\*</sup>

Heat Transfer and Thermal Power Laboratory, Department of Mechanical Engineering, Indian Institute of Technology Madras, Chennai 600 036, India

## ARTICLE INFO

### Article history:

Received 21 January 2019

Received in revised form

23 July 2019

Accepted 27 July 2019

Available online 27 July 2019

### Keywords:

Solar energy

Heat flux prediction

CPV reflective system

Non-intrusive temperature measurement

IR camera

Inverse heat transfer technique

## ABSTRACT

For a CPV system, prediction of focal flux distribution at the receiver area will give insight to more effective, energy efficient designs and to estimate power output. An experimental method for in-situ prediction of heat flux distribution profile using inverse heat transfer technique on a flat plate receiver for a CPV square parabolic dish is presented. An IR camera is used to measure the temperature of the concentrated receiver surface. The receiver domain is discretised into several heat flux elements and heat flux values for each grid is then estimated using the measured infrared (IR) pixel temperature and ordinary least square. A 3-D steady state heat conduction equation with convection and radiation heat loss boundary is regarded as the forward problem. The simulated temperatures generated from the solution of forward problem using the predicted heat flux distribution and measured temperature distribution are in close agreement. For validation purpose, the concentrated heat flux is also measured using Gardon and Schmidt-Boelter heat flux sensor. The peak predicted focal heat flux on the receiver is found to be 37.41 kW/m<sup>2</sup> whereas the heat flux value measured by the flux sensor is 39.15 kW/m<sup>2</sup> within the deviation of 4.4%.

© 2019 Elsevier Ltd. All rights reserved.

## 1. Introduction

Solar energy has a tremendous potential among all the available renewable energy technologies. With the recent advancement of development in solar energy it has now become a reliable source for power generation in our planet on par with conventional power generation technologies [1]. With further research and exploration, it can be effectively harnessed its potential with the current advanced available technology to help mankind. In today's scenario based on the demand, the solar energy can be used for electrical and thermal energy. Out of the available utilization of solar energy, concentrating solar technologies has expanded many folds and many researchers have shown great interest in expanding their work to utilize it more effectively. The capability of achieving high temperature by this technology has boosted many researchers and the efficiencies are improving enormously. Among the

concentrating solar energy technologies available there is enormous growth of Concentrating Photovoltaic (CPV) technology.

In a CPV system, the incoming solar irradiation is concentrated into a small region. Different types of optics and designs are made available in CPV depending on its application. For the existing available CPV systems, different optics, design and its limitation is provided extensively in this paper [2]. Xu et al. [3] reported to achieve an instantaneous electrical efficiency of 28% with a highest instantaneous thermal efficiency of 54% which shows that the overall efficiency of the system can be more than 80% for a CPV point focus system. Li et al. [4] presented a line focusing trough system, used CPV cells like GaAs solar cells and conventional silicon cells and proved that CPV cells are more efficient than the silicon cells in terms of thermal as well as electrical efficiencies. Fei-Lu Siaw et al. [5] shows a comprehensive study of dense-array concentrator photovoltaic system using non-imaging planar concentrator. Based on their computational modeling result, they have built a prototype of a non-imaging planar concentrator with dense array CPV cells assembly and found to achieve an experimental result with conversion efficiency of 34.18%.

In one of the CPV systems like Cassegrain optics where both the

<sup>\*</sup> Corresponding author.

<sup>\*\*</sup> Corresponding author.

E-mail addresses: [premjitmtech@gmail.com](mailto:premjitmtech@gmail.com) (N.P. Singh), [ksreddy@iitmadras.ac.in](mailto:ksreddy@iitmadras.ac.in) (K.S. Reddy).

Nomenclature	
<i>Symbols</i>	
$A$	dish area ( $\text{m}^2$ )
$C_p$	specific heat capacity ( $\text{J/kg } ^\circ\text{C}$ )
$h$	heat transfer coefficient ( $\text{W/m}^2 \text{ } ^\circ\text{C}$ )
$k$	thermal conductivity ( $\text{W/m}^\circ\text{C}$ )
$Q_c$	heat conducted ( $\text{W}$ )
$Q_h$	heat loss due to convection ( $\text{W}$ )
$Q_s$	heat stored ( $\text{W}$ )
$Q_\alpha$	heat absorbed ( $\text{W}$ )
$Q_\epsilon$	heat loss due to radiation ( $\text{W}$ )
$\hat{q}$	estimated heat flux values at each grid ( $\text{W/m}^2$ )
$T$	temperature ( $^\circ\text{C}$ )
$T_i$	temperature at $i$ th grid ( $^\circ\text{C}$ )
$T_m$	measured temperature ( $^\circ\text{C}$ )
$T_0$	initial temperature ( $^\circ\text{C}$ )
$q_j$	heat flux at $j$ th grid ( $\text{W/m}^2$ )
$t$	time (s)
$T_\infty$	ambient temperature ( $^\circ\text{C}$ )
$X$	sensitivity matrix
<i>Greek symbols</i>	
$\alpha_p$	total absorptivity
$\alpha$	absorptivity of the paint
$\lambda$	wavelength ( $\mu\text{m}$ )
$\rho$	reflectivity of the anodized aluminium
$\epsilon$	total emissivity
$\phi$	rim angle
<i>Abbreviations</i>	
APDL	Ansys Parametric Designer Language
CPV	Concentrated Photovoltaics
DC	Direct Current
DNI	Direct Normal Irradiance ( $\text{W/m}^2$ )
FEM	Finite Element Method
GPS	Global Positioning System
IR	Infrared
MS	Mild Steel
n-D	n-dimension where $n = 1,2,3$
PLC	Programmable Logic Controller
PV	Photovoltaics
<i>Subscripts</i>	
$f$	focal length
$p$	paint
$q$	heat flux values of the grids ( $\text{W/m}^2$ )

refraction and reflective types mirrors are used. It is reported that the Cassegrain system with homogenizer design combining refractive and reflective is found to increase a power output of 4.5% as compared to the ones which uses only refractive type homogenizer [6]. Different approaches are adopted by the researchers to improve the efficiency of the CPV system with optics design and also the multi-junction solar cells which are made of multi semi conductive layers [7]. For a CPV system, apart from design of optics and the precision tracking system there are some issues in the receiver which needs to be looked into like non-uniform illumination and its thermal management [8]. A proper design and thermal management for a CPV receiver is also an essential aspect as it is learnt that for every one-degree Celsius rise there is a decrease of 0.035% in efficiency [9]. In a CPV system, if the working temperature in the receiver is maintained below 80–100 °C, it can avoid degradation even if it works for a longer period with high temperatures [7]. Therefore, an effective thermal management is essential for a high concentration CPV system.

The thermal management can be carried out in two different approaches as active and passive. Royne et al. [7] provided various cooling methods that can be adopted for a CPV system. Dong et al. [10] presented a numerical study for an active cooling method with water for a novel T-shape manifold multi-channels for concentration ratio of 500 with 100 cells receiver's CPV system. From the study, it is reported that the transient analysis with double group channel network cooling design with varied solar irradiation including summer's hot weather conditions has met the cooling requirement which maintains the cells efficiency between 39.2% and 40.6%. Fins/extended surfaces with high thermal conductivity materials like copper and aluminium are commonly used in passive cooling system. However, in recent days used of Phase Change Material (PCM) are reported as one of the options for passive cooling [11–13]. For any CPV system, the receiver with the cooling system plays a vital role as it carries about 20% weightage of total cost of the system [14]. The effective design of the receiver is important in order to increase the overall efficiency of the system

[15]. Therefore, knowledge of heat flux distribution on the receiver area will give an insight for designing an effective and energy efficient one.

The flux mapping at the receiver for a CPV system or measurement of concentrated solar flux provides a very helpful information to the researchers. Numerically, the incident heat flux distribution on the receiver is often derived from modelling codes using sophisticated ray-tracing methods from the information of concentrator surface design on which solar irradiations are refracted and reflected from it [16,17]. Numerical approaches may provide fast and accurate results. However, the actual optical errors resulting from misalignment or imperfect shaping of mirrors in the concentrator are sometimes not considered. Therefore, the in-situ mapping or the measurement of the incident flux density or the heat flux distribution mapping remains an important aspect but still a challenging task. Different approaches for mapping the heat flux on the focus area like using radiometer or a similar one is provided in literature. This approach using radiometer mainly Gardon-type radiometers measures the temperature difference between the center and the circumference of the circular foil disk. The voltmeter or a data logger is used to measure the signal sent from the sensor. Then based on the respective coatings of the sensors like Zynolyte or Collodal graphite respective calibration correction factor of 0.965 and 0.782 is used. So, the method takes longer time and provides a low spatial resolution heat flux map [18–20]. The other available approach with charge-couple device (CCD) requires to keep the targeted receiver water cooled and images are recorded in gray scales. Ulmer et al. [21] reported a flux mapping system of dish/Stirling systems using CCD camera for the targeted focal spot. They have considered the calibration by calculating the total energy from the dish to the integrated gray value over the focal measurement area. The result of this indirect measuring method with the given described calibration method maps the flux distribution with high spatial resolution and good accuracy without even using a radiometer. The error of the calibration method is reported as within –2.4% and +3.8% while single

pixels are with a maximum absolute error of  $-6.15\%$  to  $+10.55\%$ .

M.R. Rodríguez-Sánchez et al. [22] provided a summarized comparisons of different experimental methods to characterize the flux distribution on the receiver surface.

Of the various approaches for heat flux mapping/predicting techniques, the inverse heat transfer method is quite an impressive approach. The main reasons are (i) the temperatures which are measured either non-intrusively or intrusively are to feed as an input for the prediction (ii) without disturbing the operation of the system, in-situ prediction can be carried out. Kant and Rudolf [23] proposed a method for determination of heat flux distributions from the measurements of surface temperatures using inverse heat transfer technique. It is shown that the surface was discretized into several heat flux elements and measured surface temperature from each discretized element used for grid by grid mapping of heat flux values. The inverse problem is then modelled using Duhamel's theorem [24–26] based on the principle of superposition, that establishes a linear relationship between measured temperature and unknown heat flux with slope as sensitivity matrix and intercept as initial temperature distribution. The sensitivity matrix is derived using the finite element scheme and heat flux value for each element is determined from the solution of system of linear equations.

Pozzobon and Salvador [27], has presented a heat flux estimation work using inverse heat transfer technique from the measured temperature through infrared camera. They have carried out the work using a concentrated solar simulator in a closed area and focal heat flux distribution at the receiver's area is mapped (grid by grid) using Duhamel's theorem which means solving the linear temperature-heat flux equation. They have made the comparison with heat flux readings from Gardon's radiometer and with the estimated results and reported to have a reasonably good agreement. Reddy et al. [28] has presented, an experimental work for in-situ prediction of heat flux distribution profile on a flat plate receiver for a refractive type CPV system using Fresnel lens. The inverse problem is formulated as parameter estimation problem with the assumption that the concentrated heat flux is of Gaussian

distribution type. The parameters of the assumed Gaussian profile are estimated from the minimization of sum of squared error between the measured and simulated temperatures using Levenberg-Marquardt algorithm. A calibrated infrared camera was used for the temperature measurement.

In literature, several numerical and experimental works are reported related to the thermal management [29,30] and electrical power output analysis [30–32] for CPV systems. In all these works, it was assumed by default that the distribution of heat flux on receiver is known in prior, which is not the case always. Therefore, in this work a prediction methodology for heat flux distribution on a flat plate receiver for a square  $3.6 \times 3.6 \text{ m}^2$  aperture area parabolic dish collector using inverse problem solution strategy is presented. In some aspects, this work is similar to the work reported in Ref. [27], however, here we have carried out the work at outdoor real-time experiment for a CPV reflective system. Also, we have adopted commercially available academic license ANSYS software for solving the forward and inverse problem.

## 2. CPV system configuration

The prediction of heat flux for the proposed work is carried out in a CPV square parabola dish collector with dual axis tracking system developed at IIT Madras, Chennai (latitude of  $12^\circ 59' 24'' \text{N}$  and longitude of  $80^\circ 13' 49'' \text{E}$ ). The system has been designed to have two symmetrical parabola dish collectors on both side of wings from the pylon. It works with both azimuth and elevation axis tracking system with a proper control system.

As shown in Fig. 1, one side of the dish is considered for the experiment to predict the focal flux heat distribution due to its symmetrical features on both side of the dish. A flat plate receiver is placed at the focal plane in one side of the dish. The temperature on the receiver area due to the concentrated solar irradiation reflected from that dish is then measured non-intrusively using a calibrated infrared camera (refer Table 1 for make and specification). Then, heat flux sensor also been used to measure the heat flux for validation purpose.

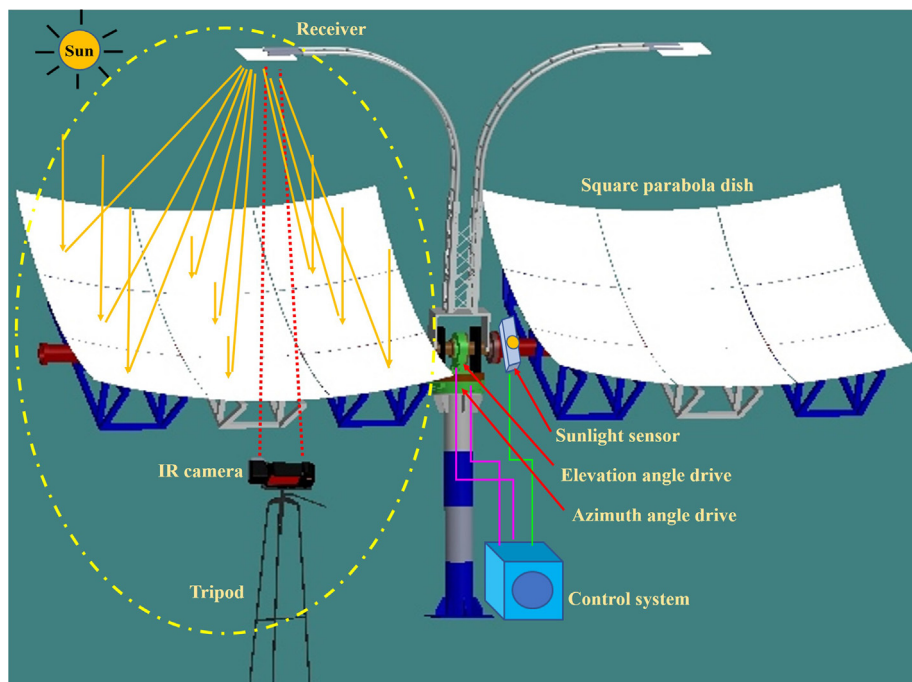


Fig. 1. Schematic of the experiment set up.

**Table 1**  
Device details and its characteristics.

Device/Sensor	Specification/Accuracy
Infrared Camera	Upto 1200 °C, Pixel size: 240 × 180
FLIR T250	±2 °C, 2%
Horizontal angle slew drive	24 VDC, <1A, electrical Gear Ratio 62:1, ≤0.20
Vertical angle slew drive	24 VDC, < 1A, electrical Gear Ratio 62:1, ≤0.20
Spectrophotometer	Wavelength accuracy (nm): UV–Visible
Agilent Cary 5000	190–900 nm: ± 0.4 nm
Pyrheliometer	Sensitivity: 12.79 μV/(W/m <sup>2</sup> )
Hukseflux	Uncertainty: 1.2%
Black Body Source	0.25% of reading or ±1 °C
Mikron M310	
Heat flux sensor	Uncertainty: < ± 6.5%
Hukseflux SBG01	
Data Logger	Uncertainty: 1 °C
KEITHLEY 2700	

The Fig. 2(a) illustrates a CPV reflective system with square parabola dish collector where the receiver is placed at the focal distance with cells arrays and PCM is used for thermal management as passive cooling. Also, the concept of the proposed experimental work using a flat plate receiver is shown in Fig. 2(b).

### 2.1. Dual axis solar tracking system

The dual axis tracker used in this work plays a very important role which tracks the sun movement accordingly. The optics of the square parabola dish is designed in such a way that the maximum percentage of the reflected solar irradiation from the dish surface to be focused on the receiver area which is placed at the focal distance.

The available CPV system is of two symmetrical square parabola dishes with the dual axis angle drives which is shown in Fig. 3. One side of the square parabola dish is of  $3.6 \times 3.6 \text{ m}^2$  aperture area. The tracking system consists of azimuth and the elevation angle slew drives which is steered by a proper control system. The slew drives are selected based on a thorough load analysis appropriate for this system. So, this tracking system which has an accuracy angle of  $1^\circ$  helps to track and locate the exact position of the Sun in the sky with an accurate angle of incidence.

#### 2.1.1. Structures of the parabola dish with dual axis tracking system

The main components of the structures are the two parabola

dishes, tracking system such as azimuthal and elevation angle slew drives, supporting structure for the receiver and the control system. The reflective area of the parabola dish is of anodized aluminum sheets with a thickness of 0.4 mm and it's reflectivity of 0.9 as per the supplier's specification. The same also cross-checked with a sample measured at Spectrophotometer (refer Table 1 for make and specification). The focal length ( $f$ ) of the parabola dish is calculated from Eq. (1) with a rim angle ( $\phi$ ) of  $36.6^\circ$  and the aperture area ( $a$ ) is of  $3.6 \times 3.6 \text{ m}^2$  [33].

$$\tan \phi = \left\{ \frac{8 \left( \frac{f}{a} \right)}{16 \left( \frac{f}{a} \right)^2 - 1} \right\} \quad (1)$$

The parabola profile of the dish is then generated using the Eq. (2) and the plot between  $x$  and  $y$  values is shown in Fig. 4(a).

$$y = \frac{x^2}{4f} \quad (2)$$

From the generated parabola dish, the square shape with aperture area of  $3.6 \times 3.6 \text{ m}^2$  is truncated and is designed to use the plain reflective anodized aluminium sheets instead of three-dimensional glass mirrors with 9 facets. So, the parabolic profile of the dish has been developed from the shape of the supporting arms of six numbers with reference to the torque tube surface where the supporting arms are screwed. The photograph of the fabricated square parabola dish is shown in Fig. 4(b). The receiver's supporting structure is designed with adjustable screws in both vertical and horizontal directions in order to adjust the spillage losses on the focus area. The concentration ratio between the dish area of  $3.6 \times 3.6 \text{ m}^2$  and the receiver area of  $0.4 \times 0.4 \text{ m}^2$  is 81. So, when the dish is placed in the Sun's position, the reflected incoming solar irradiation from dish will be concentrated on the receiver area. The pylon, which is taking the entire load of the system is designed with proper factor of safety and placed with properly screwed base. The slew drives are mounted over the top of the pylon with a proper safety. Apart from the slew drives, all the parts are made of mild steels and are powder coated in order to improve corrosion resistance. The sunlight sensors give feedback to the control system of the tracking system are properly aligned and fixed to the torque tube.

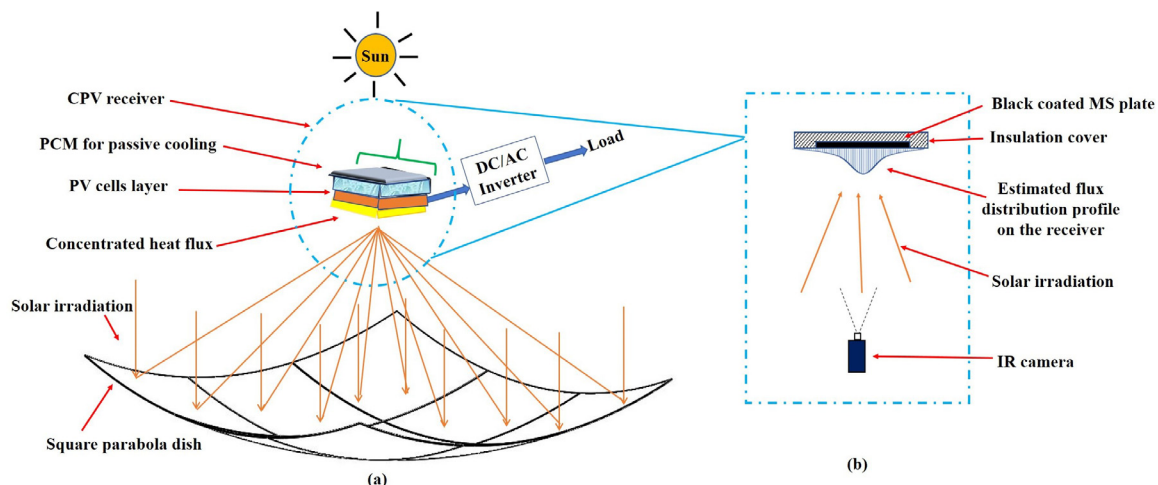


**Fig. 2.** (a) Schematic showing the illustration of a CPV receiver cells array with PCM cooling (b) Schematic showing the concept of the proposed work for focal heat flux prediction.

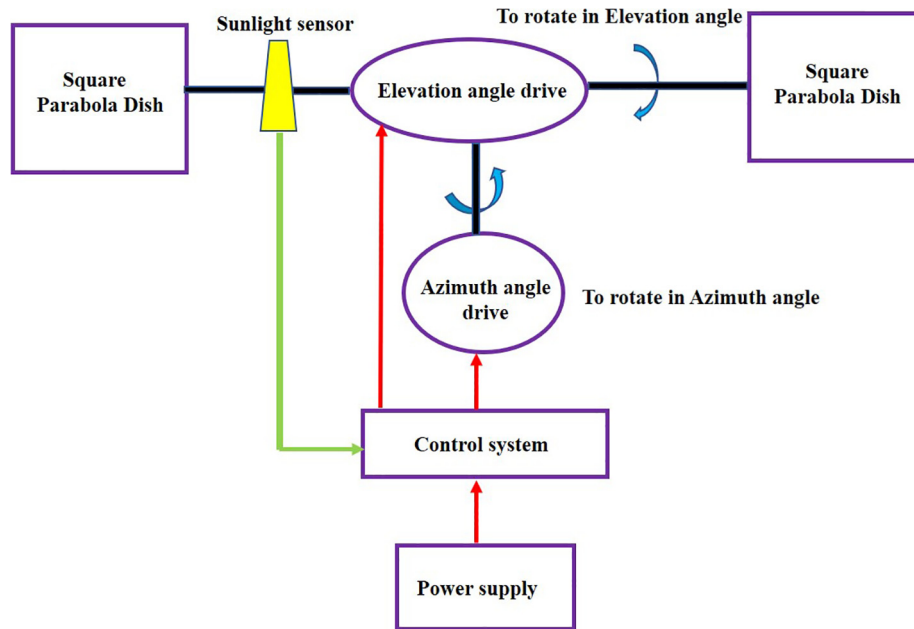


Fig. 3. Schematic illustration of the available CPV system with dual axis tracking.

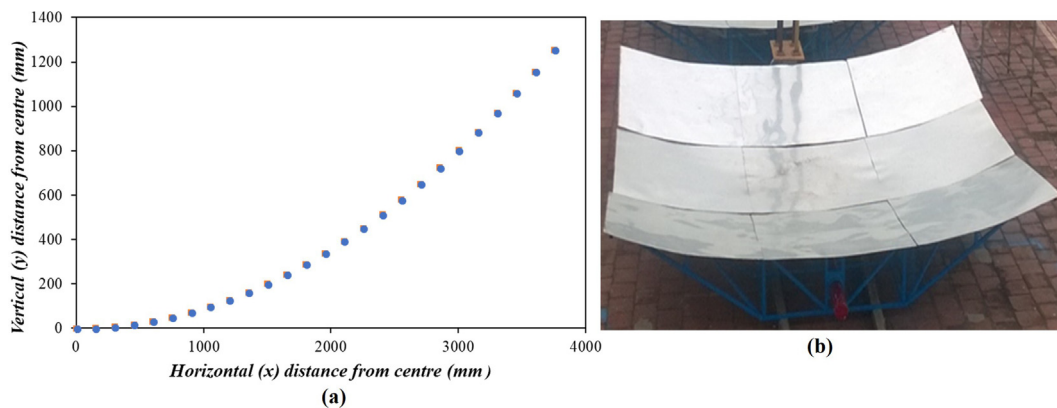


Fig. 4. (a) Design profile of the parabola dish (b) Photograph of the truncated square parabolic dish of aperture area  $3.6 \times 3.6 \text{ m}^2$ .

### 2.1.2. Control system of the dual axis tracker

This unit consists of PLC, motors and worm gears for azimuth and elevation drives, sunlight sensors, position sensors, encoders and power relays. The CPV dish installation site information like latitude and longitude, computed sun-ephemeris were fed and programmed.

The annual movement of the Sun's motion is detected through a position sensor installed in this control system. The tracking time is then fed through a battery-backed clock connected to the PLC. Sunlight sensor which is attached to the torque tube measures the light intensity. Based on the information fed from the sensors and encoders, the PLC commands DC motors to control azimuth and elevation angles of the CPV system, in such a way the dishes are always kept perpendicular to the Sun. This unit helps to track the Sun's position at any time of the day accordingly the incoming irradiation falling on the dish will be reflected and concentrated to the receiver area. Provision of manual switches are also kept in the control system which uses at the time of fixing receivers, proper parking after the experimentation also in case of emergency when automatic control fails while operating.

### 2.2. Receiver for the proposed work

In this work, a flat plate made of MS is used instead of the actual PV receiver for the real time experiment and the analysis is carried out accordingly. The MS plate (hereafter called receiver) with a dimension of  $40 \text{ cm} \times 40 \text{ cm} \times 0.2 \text{ cm}$  is fabricated on the ceramic fiber insulation of  $50 \text{ cm} \times 50 \text{ cm} \times 2 \text{ cm}$  as shown in Fig. 5. The ceramic fiber insulation material used has a low thermal conductivity ( $k = 0.5 \text{ W/mK}$ ) in order to minimize the heat loss because of convection and radiation. The MS plate area is painted with high temperature heat resistant black paint to enhance its absorptivity.

One of the essential parameters for this work is the surface emissivity of the receiver was measured using spectrophotometer (refer Table 1 for make and specification). A standard sample (as per the spectrophotometer's specification) made up of Mild Steel (MS) was coated with the same paint for measuring the optical properties. The visible wavelength range of 300 nm up to 800 nm was selected and measured the spectral transmittivity and reflectivity values. Applying the equation  $\rho_\lambda + \alpha_\lambda + \tau_\lambda = 1$ , the measured values of spectral transmittivity and reflectivity, the spectral

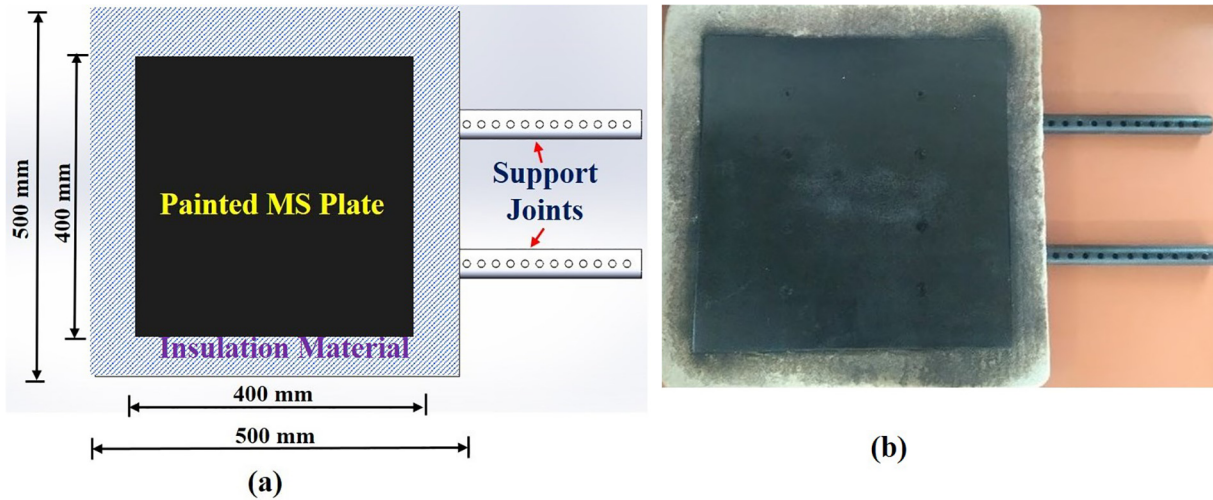


Fig. 5. (a) Schematic of the receiver (b) Picture taken of the actual receiver taken after the experiment.

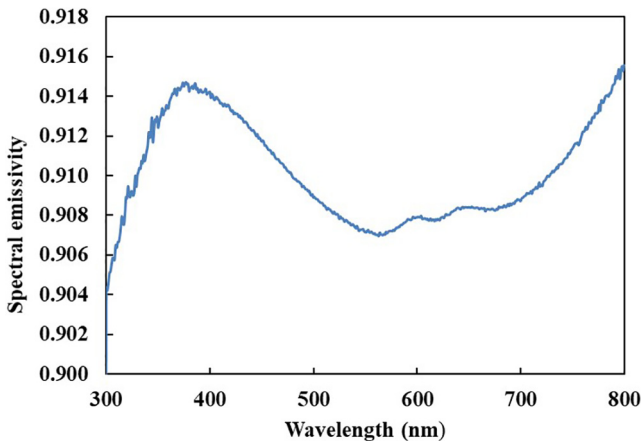


Fig. 6. Spectral emissivity of the paint.

absorptivity is calculated. Using the Kirchhoff's law  $\alpha_\lambda = \epsilon_\lambda$ , the spectral emissivity may be obtained which is shown in Fig. 6. Integrating the spectral emissivity values from  $\lambda = 300$  to  $\lambda = 800$  nm, the hemispherical total emissivity is computed and obtained as

0.91.

### 3. Experiment procedure for non-intrusive temperature measurement

The experiment for this proposed work was started during noon time of the day. At first, the dual-axis tracker was turned on and tracked using manual mode and position down in such a way that the receiver can be placed to the mounting structure. The supporting structures for mounting the receiver was designed in order to accommodate the receiver in the focal area with respect to the focal distance (Refer Fig. 1.) for schematic of the square parabola concentrator with dual axis tracking system.

The receiver is aligned accordingly in the mounting structure and properly placed and fixed with necessary nuts and bolts at the focal distance of the concentrator at 2.8 m as shown in Fig. 7(a).

Prior experiments conducted using high temperature ceramic pad for checking the theoretical focal distance and alignments for fixing the receiver plate is shown in Fig. 7 (b).

Then, the tracker is turned on to the automatic dual axis mode to track the exact position of the Sun. The IR camera (refer Table 1 for make and specification) was aligned and placed with a proper height from the ground to ensure the operating range is within the

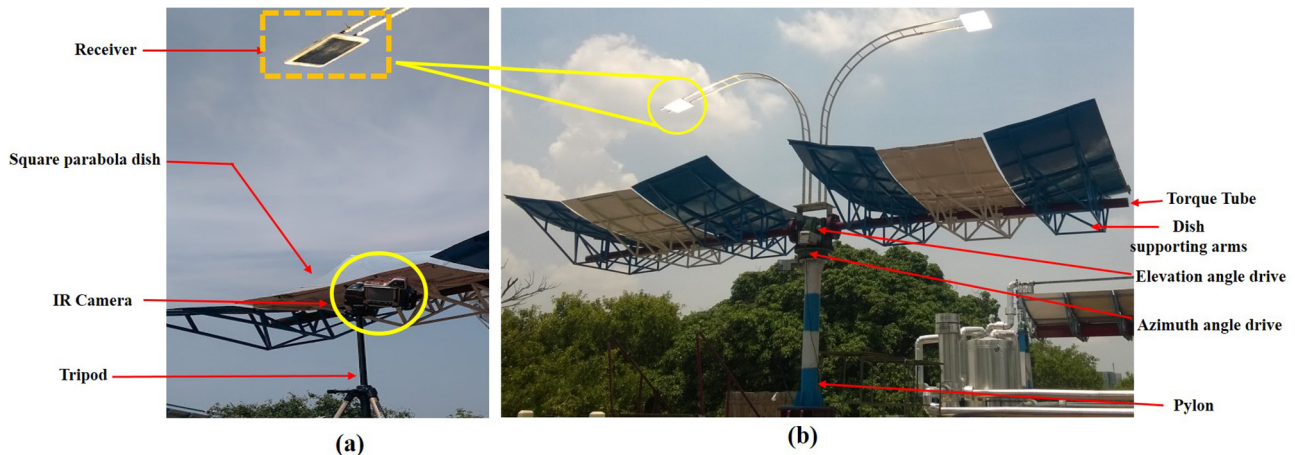


Fig. 7. (a) Photograph taken at the time of experiment (b) Focal plane experiments conducted prior to the proposed work.

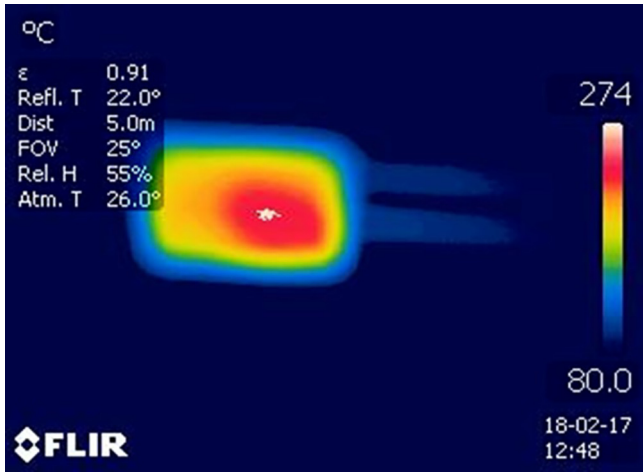


Fig. 8. IR image of the receiver surface captured during experiment.

permissible limits. The IR camera was calibrated before by the standard method of comparison with a highly accurate black body source. Since, the sole purpose of this work is to predict the heat flux distribution mapping of this CPV system. The detailed information about the calibration procedure using a highly accurate black body source (refer Table 1 for make and specification) of the IR camera is not presented here. However, it is provided in the reference [28]. The emissivity value of the black painted receiver surface is calculated as 0.91. The detailed information of the emissivity calculation using spectrophotometer is given in Section 2.2. Once, the square concentrator is focused to the Sun, the IR images of the receiver were recorded continuously in a laptop.

The captured IR image is provided in Fig. 8, found that the temperature has raised above 250 °C. One important point to be noted here is that placing the IR camera exactly perpendicular to the receiver will hinder the reflected solar rays falling on the receiver. Therefore, IR camera is placed and aligned in an angle but within the permissible operating range of 5m from receiver.

The error involved in temperature measurement because of positioning IR camera away from the receiver has been taken care at the time of converting radiometric information into the pixel temperature data. Also, an error due to reflected temperature from

the surroundings is nullified in a similar way as discussed in Ref. [27]. During the course of experiment the DNI was also measured every second using an accurate pyrheliometer which is shown in Fig. 9. The corresponding DNI for the particular IR image as shown in Fig. 8 (used in inverse analysis for heat flux estimation) was found to be 650 W/m<sup>2</sup>. Also, the other parameters like ambient temperature and wind speed were obtained from the weather monitoring system.

### 3.1. Heat flux measurement using flux sensor

Heat flux was also measured using an accurate heat flux sensor on the subsequent day of non-intrusive temperature measurement. The heat flux sensor was mounted at the same focal distance on the same side of the concentrator dish. The heat flux values were recorded continuously using data logger. Fig. 10, shows the heat flux sensor mounted on the frame of receiver area.

The heat flux sensor (thermopile sensor) works with the principle of both Gardon and Schmidt-Boelter technology. Operating range of this sensor is (5–200) × 10<sup>3</sup> W/m<sup>2</sup>. Sensor's surface is black-coated, which absorbs all irradiation and with a flat spectrum range of 300 to 50,000 nm range and has a near-perfect cosine response. The thermopile sensor absorbs the irradiation due to the black coating and generates a voltage output signal that is proportional to the heat flux. The output voltage signal is then converted using data logger which is proportional to the heat flux. Simultaneously, the DNI values were also measured every second using the pyrheliometer. These measurements can be used to validate the results estimated from the inverse heat transfer method. Here, the measured peak heat flux value corresponding to the DNI of 650 W/m<sup>2</sup> has been considered to compare with the estimated heat flux from inverse heat transfer.

## 4. Mathematical formulation

### 4.1. Forward model

The solar irradiation falling on the parabolic dish collector is concentrated onto the receiver plate as shown in Fig. 7. The mathematical model for heat transfer in the receiver plate due to the concentrated heat flux may be modelled by considering an elemental volume as shown in Fig. 11. The energy balance for the considered elemental volume of the receiver can be written as in

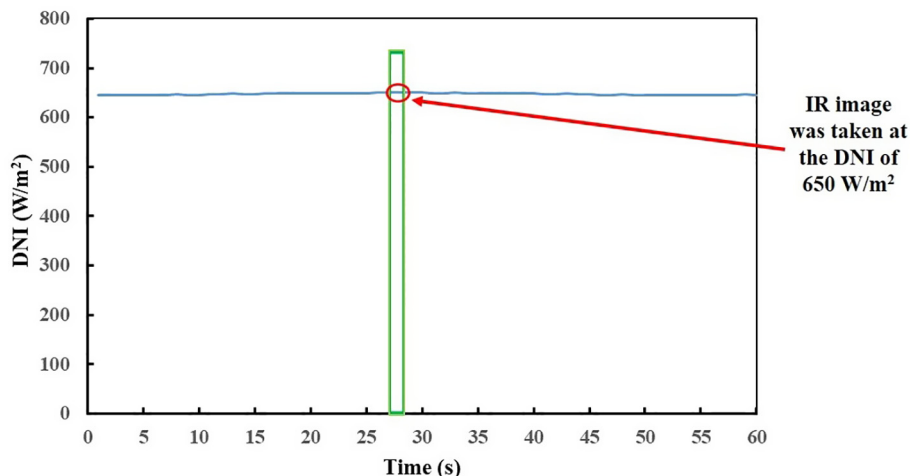


Fig. 9. DNI vs Time during the experiment.

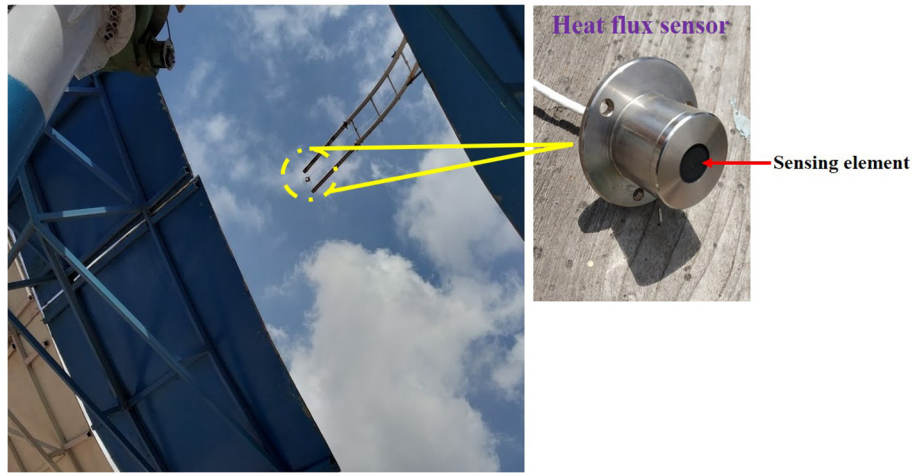


Fig. 10. Heat flux sensor used for measurement of flux.

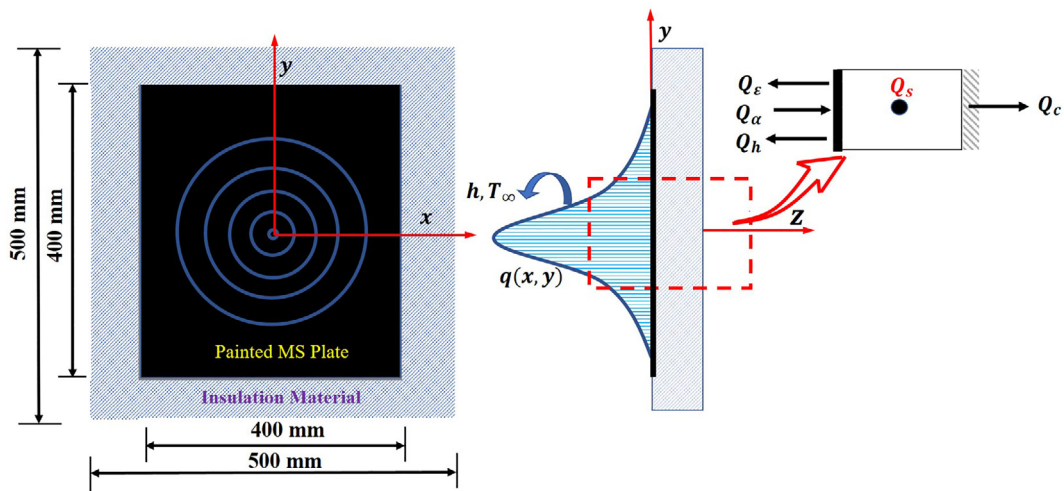


Fig. 11. Energy balance on the receiver due to concentrated heat flux.

Eq. (3).

$$Q_\alpha + Q_c - Q_h - Q_e = Q_s \tag{3}$$

Substituting conductive, convective and radiative terms in the Eq. (3), one may obtain the mathematical model for the actual heat transfer in the receiver as given in Eq. (4).

$$\alpha_p q(x,y) + k \left( \frac{\partial^2 T}{\partial x^2} + \frac{\partial^2 T}{\partial y^2} + \frac{\partial^2 T}{\partial z^2} \right) - h(T - T_\infty) - \sigma \epsilon_p (T^4 - T_\infty^4) = \rho C_p \frac{\partial T}{\partial t} \tag{4}$$

Where T is in Kelvin and  $\sigma$  is the Stefan-Boltzmann constant =  $5.67 \times 10^{-8} (\text{W/m}^2 \text{K}^4)$ .

Without loss of generality, the heat transfer within the receiver can be considered as steady-state as the receiver attains steady-state condition within few seconds as soon as it is exposed to concentrated heat flux as discussed in Ref. [34]. Fig. 12 shows

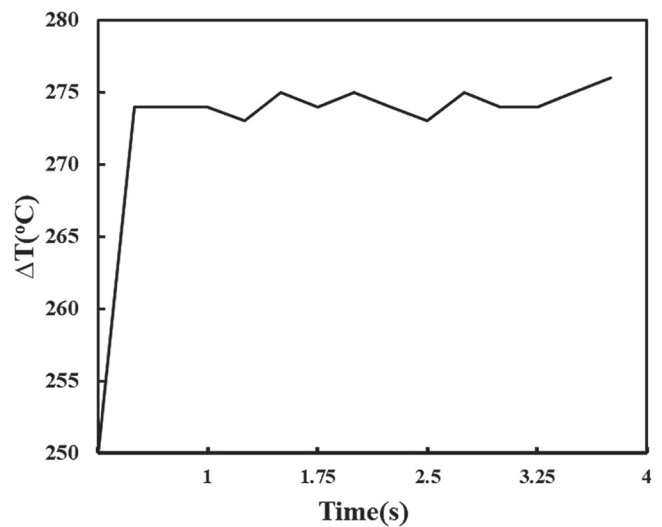


Fig. 12. Transient response of the receiver for the concentrated heat flux.

measured transient temperature response of the receiver from the instant when it is subjected to concentrated solar irradiation. From this figure, it is clearly evident that there is a sharp rise of temperature within fraction of seconds and thereafter the temperature remains steady. Therefore, it is reasonable to assume steady heat transfer and Eq. (4) can be re-written as given in Eq. (5).

Since the receiver plate is fixed within low thermal conductivity ceramic insulation (refer Fig. 5), it can be reasonably assumed adiabatic boundary condition on all the boundaries.

$$\alpha_p q(x,y) + k \left( \frac{\partial^2 T}{\partial x^2} + \frac{\partial^2 T}{\partial y^2} + \frac{\partial^2 T}{\partial z^2} \right) - h(T - T_\infty) - \sigma \epsilon_p (T^4 - T_\infty^4) = 0 \tag{5}$$

The solution of Eq. (5), for temperature distribution with known thermal conductivity and boundary conditions is known as forward problem. However, in some cases, there may arise a situation where the objective may be to predict the boundary condition as in this case. This class of problem is called the inverse problem. In general, measured quantities (temperature in this case) are used to solve the inverse problem. Naturally, the inverse problems are ill-posed in nature due to error in the measured temperatures and lack of sensitivity of unknowns. Various approaches are available in literature [24–26] to overcome the issue due to ill-posedness of the inverse problem.

#### 4.2. Inverse model

Inverse problems are broadly classified into two categories as (1) design problem and (2) identification problem [35]. The inverse design problem deals with the prediction/estimation of distribution and strength of heat source and boundary conditions [27,28] whereas inverse identification problem deals with the estimation of thermo-physical properties [36]. In literature, both design and identification problems are formulated as parameter estimation and function estimation problem. For example, Reddy et al. [28] adopted inverse parameter estimation strategy to solve inverse design problem whereas in Refs. [23,27] similar inverse design

problem is solved using function estimation strategy.

In this work, function estimation strategy to predict the heat flux distribution on the receiver plate was adopted. The idea here is to map the grid-by-grid heat flux values through minimization of error square between the measured and simulated temperature distribution which is as similar in Ref. [27]. Mathematically, the inverse problem can be represented as given in Eq. (6).

$$S^2 = \sum_j \sum_i [T_m^{ij} - T^{ij}(\hat{q})]^2 \tag{6}$$

Here,  $\hat{q}$  is the estimated heat flux,  $T_m^{ij}$  and  $T^{ij}(\hat{q})$  are the measured and simulated temperatures respectively at  $(i,j)^{th}$  grid location. The minimization of above equation corresponds to the estimated heat flux values at each grids of the receiver domain. The minimization can be achieved through ordinary least-square technique, since the considered estimation problem is linear with respect to unknowns. The ordinary least-square for this estimation problem can be conveniently written as given in Eq. (7).

$$\hat{q} = [X'X]^{-1} X'T_m \tag{7}$$

Here,  $X$  is the sensitivity matrix whose elements are composed of sensitivity coefficient of unknown parameters. The sensitivity coefficient of a parameter is defined as the change in temperature for a small perturbation in the unknown parameter. The mathematical definition of sensitivity coefficient is given in Eq. (8). As mentioned earlier, IR camera is used to measure the temperature which gives multiple temperature points. The receiver domain is also discretized into number of grids, equal to the number of available measured temperature points.

$$X = \frac{\partial T}{\partial q} \tag{8}$$

The  $(i,j)^{th}$  element of sensitivity matrix corresponds to partial derivative in temperature of the receiver domain for a small perturbed change in heat flux value of the same element. Each element of the sensitivity matrix can be represented as shown in Eq. (9).

$$X = \begin{bmatrix} \left( \begin{matrix} T_{1,j} & \dots & T_{1,n} \\ \vdots & \ddots & \vdots \\ T_{m,1} & \dots & T_{m,n} \end{matrix} \right)_{1,j}^{q+\delta q} - \left( \begin{matrix} T_{1,j} & \dots & T_{1,n} \\ \vdots & \ddots & \vdots \\ T_{m,1} & \dots & T_{m,n} \end{matrix} \right)_{1,j}^q & \dots & \left( \begin{matrix} T_{1,j} & \dots & T_{1,n} \\ \vdots & \ddots & \vdots \\ T_{m,1} & \dots & T_{m,n} \end{matrix} \right)_{1,n}^{q+\delta q} - \left( \begin{matrix} T_{1,j} & \dots & T_{1,n} \\ \vdots & \ddots & \vdots \\ T_{m,1} & \dots & T_{m,n} \end{matrix} \right)_{1,n}^q \\ \partial q_{1,j} & & \partial q_{1,n} \\ \vdots & \ddots & \vdots \\ \vdots & & \vdots \\ \left( \begin{matrix} T_{1,j} & \dots & T_{1,n} \\ \vdots & \ddots & \vdots \\ T_{m,1} & \dots & T_{m,n} \end{matrix} \right)_{m,1}^{q+\delta q} - \left( \begin{matrix} T_{1,j} & \dots & T_{1,n} \\ \vdots & \ddots & \vdots \\ T_{m,1} & \dots & T_{m,n} \end{matrix} \right)_{m,1}^q & \dots & \left( \begin{matrix} T_{1,j} & \dots & T_{1,n} \\ \vdots & \ddots & \vdots \\ T_{m,1} & \dots & T_{m,n} \end{matrix} \right)_{m,n}^{q+\delta q} - \left( \begin{matrix} T_{1,j} & \dots & T_{1,n} \\ \vdots & \ddots & \vdots \\ T_{m,1} & \dots & T_{m,n} \end{matrix} \right)_{m,n}^q \\ \partial q_{m,1} & & \partial q_{m,n} \end{bmatrix} \tag{9}$$

Here (m,n) corresponds to number of grid points in (x,y) directions respectively. The computation of sensitivity matrix is discussed in the following section.

## 5. Solution methodology

In this work, Finite Element Method (FEM) based commercial software ANSYS Mechanical 18.2 (Academic license) is used to solve the Eq. (5) and find the temperature distribution with given thermal conductivity and boundary conditions. A solid thermal element-solid90 with 20 nodes [37] is used to discretize the solution domain. The heat flux to each grid is applied as elemental surface load. An APDL program is written to automate the geometry creation, material property assigning, meshing, applying boundary condition and solution. The nodal temperature results are saved in an editable file which are then post-processed in MATLAB to obtain temperature contours with respect to geometrical coordinate. Also, MATLAB code is written to calculate the sensitivity matrix as follows: at first temperature distribution ( $T_q$ ) is obtained with some realistic heat flux values to each grid. Then, heat flux value of each grid is perturbed by a small value ( $\delta q$ ) and the forward problem is solved for temperature distribution ( $T_{q+\delta q}$ ). Sensitivity matrix is then calculated using the finite difference scheme as shown in Eq. (9). Once the sensitivity matrix is computed, the unknown heat flux values of each grid can be estimated from the solution of Eq. (7). The methodology adopted for the proposed work of grid by grid

mapping of heat flux on the receiver plate is represented in the form of flowchart and is shown in Fig. 13.

## 6. Results and discussion

The numerical estimation with synthetic measured temperature data was carried out before proceeding to estimate grid by grid heat flux values with the measured temperature. The synthetic data is generated by adding additive and uncorrelated random errors with zero mean and known standard deviation to the solution of forward problem. To generate the synthetic temperature data, forward problem is solved with Gaussian-distributed heat flux on the receiver. Based on grid independent study, the receiver domain is discretized into  $40 \times 40$  heat flux elements. Fig. 14 (a) shows actual distribution of heat flux that was used to solve the forward problem and Fig. 14 (b) shows the grid by grid estimated heat flux values using synthetic temperature data.

A comparison between the exact and grid by grid estimated heat flux values shows that the proposed approach can be successfully employed in real time applications such as in this case for predicting solar concentrated heat flux distribution on the receiver area. The actual captured IR image of the receiver surface is shown in Fig. 8. Then, this radiometric image is converted into pixel temperature data using FLIR ThermoCAM Researcher Pro 2.10 (30 days trial version).

The temperature contour of the receiver surface is shown in Fig. 15. Note that, only the temperature of receiver region is shown

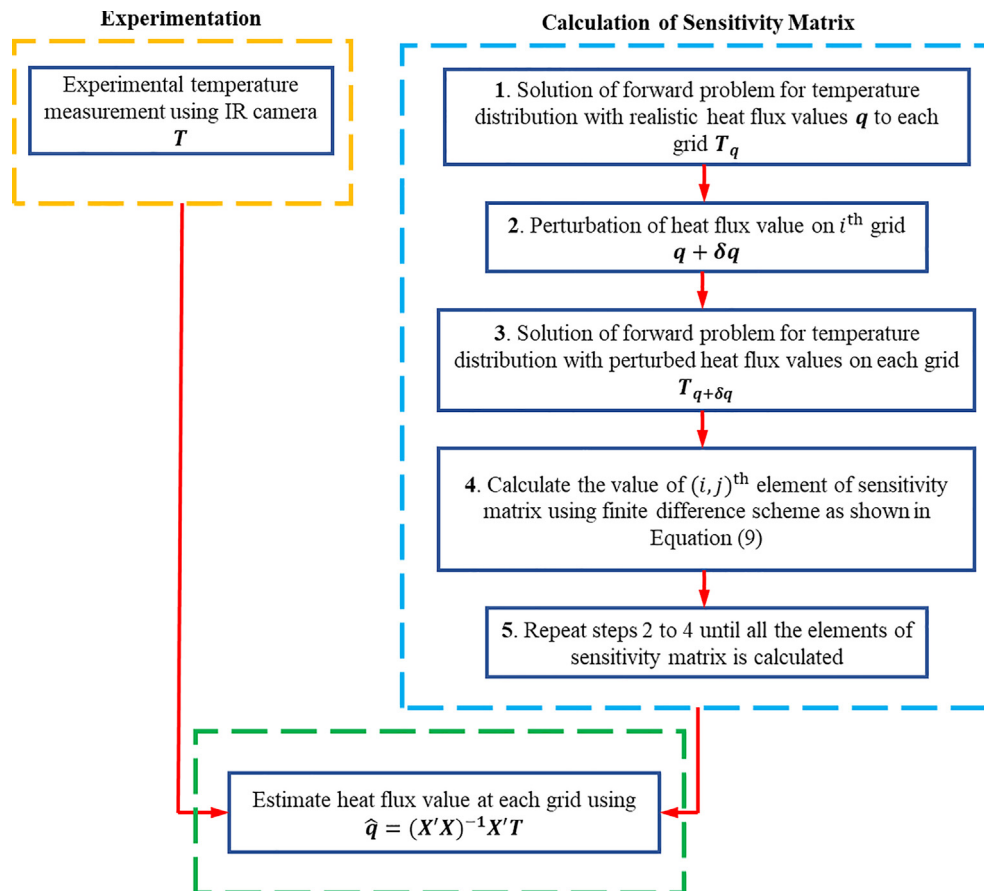


Fig. 13. Flowchart of estimation of heat flux distribution using Inverse heat transfer technique.

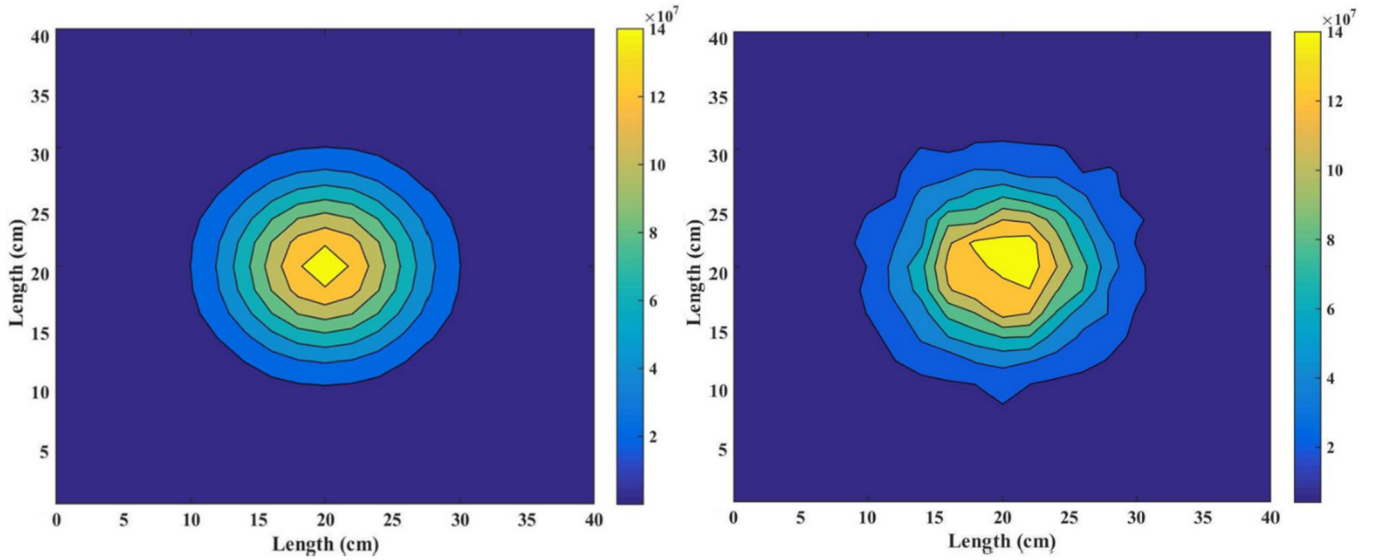


Fig. 14. (a) Assumed heat flux distribution in  $W/m^2$  for generation of synthetic experimental temperature data (b) Estimated heat flux distribution in  $W/m^2$  with the proposed inverse method and synthetic temperature data.

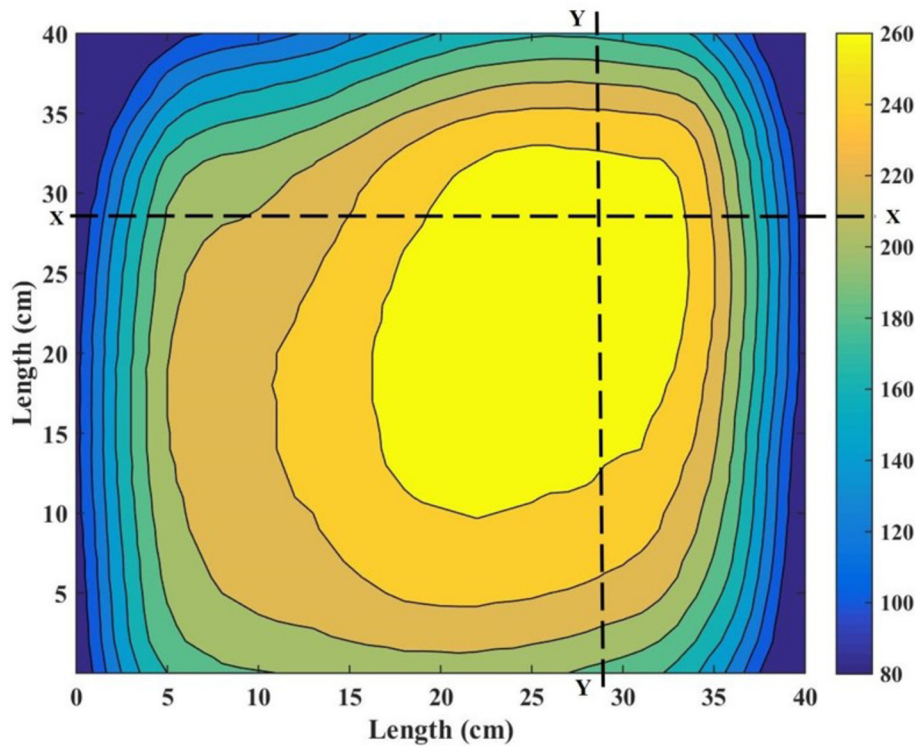


Fig. 15. Pixel by pixel temperature data of the captured IR image.

in the Fig. 15. Also, it is noteworthy to mention here that the concentrated heat spot is not at the exact center of the receiver. The reason may be because of some error in tracking system, slight misalignment of receiver from its actual position in the receiver supporting structures.

Now, this pixel temperature is used to estimate heat flux value of the discretized elements. Since, the maximum temperature attained is greater than  $250^\circ C$ , the thermal conductivity of MS receiver plate is considered as function of temperature as given in

Eq. (10) [38].

$$k(T) = 60.584 + 0.0515T - 3 \times 10^{-5}T^2 \text{ W/mK} \quad (10)$$

The convective heat loss coefficient appearing in the forward problem is calculated using the correlation given in Eq. (11) [39] for the geometrical orientation and wind velocity during experiment. Fig. 16 shows the estimated grid by grid heat flux values of the receiver plate.

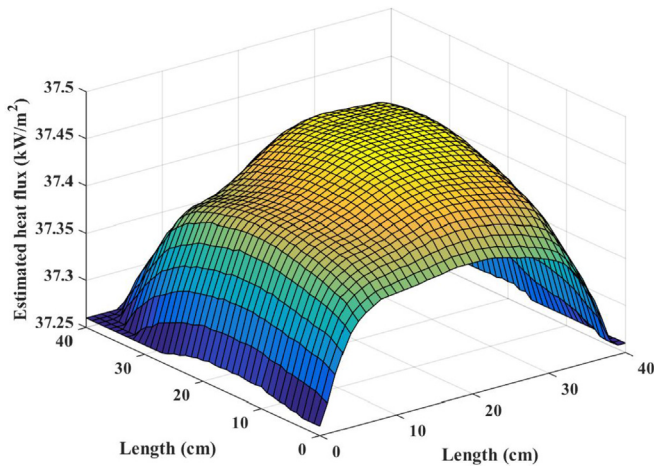


Fig. 16. Estimated grid by grid flux distribution with the proposed inverse method and measured IR pixel temperature.

$$h = (6.63 \pm 0.05) + (3.87 \pm 0.13) \times V^{0.8} \times L^{-0.2}, \text{ for } V \leq 1.12 \text{ m/s} \tag{11}$$

Now, the forward problem is solved for temperature distribution with the estimated heat flux distribution. A comparison between the simulated temperature and measured temperature along the X-X and Y-Y axis of the receiver plate is shown in Fig. 17 (a) and (b) respectively. Note that X-X and Y-Y line does not pass through the central axis, instead it was chosen at random locations and there is no specific reason for choosing these axis lines randomly. The locations of X-X and Y-Y are shown in Fig. 15.

It is evident from the Fig. 17 (a) and (b) that simulated temperatures are in close agreement with the measured temperatures. The peak value of mapped heat flux with the proposed method is 37.41 kW/m<sup>2</sup> from the IR image of Fig. 8 with the corresponding recorded instant DNI value of 650 W/m<sup>2</sup>. Also, from the subsequent day experiments of using flux sensor, heat flux value corresponding to the DNI of 650 W/m<sup>2</sup> is found to be 39.15 kW/m<sup>2</sup>. The deviation

between the estimated peak heat flux and measured heat flux is found as 4.4%.

### 7. Conclusions

In this paper, a methodology was proposed to predict the focal flux heat distribution of a CPV reflective system using inverse heat transfer technique. The work was carried out in a CPV 3.6 × 3.6 m<sup>2</sup> square parabola dish collector with dual axis tracking system. An inverse function estimation strategy was adopted in which the receiver domain was discretized into several heat flux elements and the corresponding heat flux values of each elements was estimated using measured IR temperature. Initially, the prediction was carried out with numerical estimation with synthetic measured temperature data. Later, concentrated heat distribution was mapped grid by grid using the actual measured temperature. The plots between the measured and simulated temperatures obtained with the estimated heat flux distribution were in good agreement. The peak predicted heat flux was found to be 37.41 kW/m<sup>2</sup> whereas the heat flux value measured by heat flux sensor was 39.15 kW/m<sup>2</sup>. The deviation between the predicted peak heat flux and the measured heat flux was found to be less than 5%. This shows the close agreement between the estimated peak and the measured heat flux by the sensor and clearly confirms the validity of the proposed method. Therefore, the predicted heat flux can be used as an input parameter for the thermal analysis of the receiver and subsequently to predict the power output of the CPV system. This particular approach is inexpensive and used of basic inverse heat transfer method has a good merit. In other techniques like using CCD camera, a high-end water-cooled target is used and relies significantly on the external scaling factor applied to the captured grey images, mostly from the external measurement of radiometric readings. As an important takeaway from the present proposed work, in-situ prediction of the heat flux distribution on the CPV receiver without disturbing the system operation is of great merit and it shall attract researchers to adopt the methodology in a similar fashion, into other important concentrating solar systems such as linear Fresnel reflector (LFR), parabolic trough, central tower, etc.

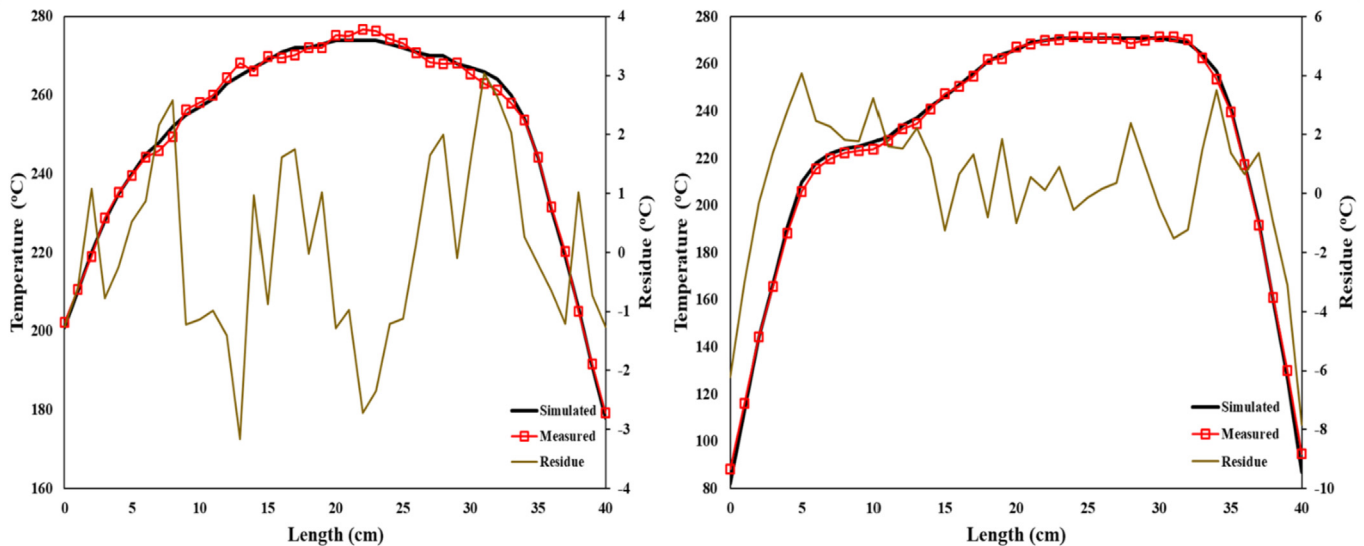


Fig. 17. Measured temperature vs simulated temperature along (a) X-X axis and (b) Y-Y axis as shown in Fig.15.

## Acknowledgement

The financial support provided by Department of Science and Technology (DST, Govt. of India), New Delhi through the research project (Grant No. DST/TM/CERI/D22(C) and Grant No. DST/IMP/UK/P-137/2016) are duly acknowledged. Also, the authors would like to thank Dr. Somasundaram S, Research Associate, Department of Mechanical Engineering for his support during experiments and the insightful discussions.

## References

- [1] N.S. Lewis, Solar energy use 798 (2013) 798–802, <https://doi.org/10.1126/science.1137014>.
- [2] K. Shanks, S. Senthilarasu, T.K. Mallick, Optics for concentrating photovoltaics: trends, limits and opportunities for materials and design, *Renew. Sustain. Energy Rev.* 60 (2016) 394–407, <https://doi.org/10.1016/j.rser.2016.01.089>.
- [3] N. Xu, J. Ji, W. Sun, L. Han, H. Chen, Z. Jin, Outdoor performance analysis of a 1090× point-focus Fresnel high concentrator photovoltaic/thermal system with triple-junction solar cells, *Energy Convers. Manag.* 100 (2015) 191–200, <https://doi.org/10.1016/j.enconman.2015.04.082>.
- [4] M. Li, G.L. Li, X. Ji, F. Yin, L. Xu, The performance analysis of the trough concentrating solar photovoltaic/thermal system, *Energy Convers. Manag.* 52 (2011) 2378–2383, <https://doi.org/10.1016/j.enconman.2010.12.039>.
- [5] F.L. Siaw, K.K. Chong, C.W. Wong, A comprehensive study of dense-array concentrator photovoltaic system using non-imaging planar concentrator, *Renew. Energy* 62 (2014) 542–555, <https://doi.org/10.1016/j.renene.2013.08.014>.
- [6] K. Shanks, H. Baig, N.P. Singh, S. Senthilarasu, K.S. Reddy, T.K. Mallick, Prototype fabrication and experimental investigation of a conjugate refractive reflective homogeniser in a cassegrain concentrator, *Sol. Energy* 142 (2017) 97–108, <https://doi.org/10.1016/j.solener.2016.11.038>.
- [7] A. Roynce, C.J. Dey, D.R. Mills, Cooling of photovoltaic cells under concentrated illumination: a critical review, *Sol. Energy Mater. Sol. Cells* 86 (2005) 451–483, <https://doi.org/10.1016/j.solmat.2004.09.003>.
- [8] J.S. Coventry, Performance of a concentrating photovoltaic/thermal solar collector, *Sol. Energy* 78 (2005) 211–222, <https://doi.org/10.1016/j.solener.2004.03.014>.
- [9] L. Micheli, N. Sarmah, X. Luo, K.S. Reddy, T.K. Mallick, Design of a 16-cell densely-packed receiver for high concentrating photovoltaic applications, *Energy Procedia* 54 (2014) 185–198, <https://doi.org/10.1016/j.egypro.2014.07.262>.
- [10] J. Dong, X. Zhuang, X. Xu, Z. Miao, B. Xu, Numerical analysis of a multi-channel active cooling system for densely packed concentrating photovoltaic cells, *Energy Convers. Manag.* 161 (2018) 172–181, <https://doi.org/10.1016/j.enconman.2018.01.081>.
- [11] M.C. Browne, B. Norton, S.J. McCormack, Phase change materials for photovoltaic thermal management, *Renew. Sustain. Energy Rev.* 47 (2015) 762–782, <https://doi.org/10.1016/j.rser.2015.03.050>.
- [12] M. Emam, M. Ahmed, Cooling concentrator photovoltaic systems using various configurations of phase-change material heat sinks, *Energy Convers. Manag.* 158 (2018) 298–314, <https://doi.org/10.1016/j.enconman.2017.12.077>.
- [13] D. Li, Y. Xuan, E. Yin, Q. Li, Conversion efficiency gain for concentrated triple-junction solar cell system through thermal management, *Renew. Energy* 126 (2018) 960–968, <https://doi.org/10.1016/j.renene.2018.04.027>.
- [14] M.C. Extance A, *The Concentrated Photovoltaics Industry Report 2010*, CPV Today, 2010 (n.d).
- [15] T. Concentrated, P. Industry, *The Concentrated Photovoltaics Industry Report 2010 the Concentrated Photovoltaics Industry Report 2010*, 2010.
- [16] G.S. Chaitanya Prasad, K.S. Reddy, T. Sundararajan, Optimization of solar linear Fresnel reflector system with secondary concentrator for uniform flux distribution over absorber tube, *Sol. Energy* 150 (2017) 1–12, <https://doi.org/10.1016/j.solener.2017.04.026>.
- [17] S.R. Pavlovic, V.P. Stefanovic, Ray tracing study of optical characteristics of the solar image in the receiver for a thermal solar parabolic dish collector, *J. Sol. Energy* 2015 (2015) 326536, <https://doi.org/10.1155/2015/326536> (10 pp.).
- [18] J. Llorente, J. Ballestrín, A.J. Vázquez, A new solar concentrating system: description, characterization and applications, *Sol. Energy* 85 (2011) 1000–1006, <https://doi.org/10.1016/j.solener.2011.02.018>.
- [19] D.S. Codd, A. Carlson, J. Rees, A.H. Slocum, A low cost high flux solar simulator, *Sol. Energy* 84 (2010) 2202–2212, <https://doi.org/10.1016/j.solener.2010.08.007>.
- [20] J. Ballestrín, C.A. Estrada, M. Rodríguez-Alonso, C. Pérez-Rábago, L.W. Langley, A. Barnes, Heat flux sensors: calorimeters or radiometers? *Sol. Energy* 80 (2006) 1314–1320, <https://doi.org/10.1016/j.solener.2006.03.005>.
- [21] S. Ulmer, W. Reinalter, P. Heller, E. Lüpfer, D. Martínez, Beam characterization and improvement with a flux mapping system for dish concentrators, *J. Sol. Energy Eng.* 124 (2002) 182, <https://doi.org/10.1115/1.1464881>.
- [22] M.R. Rodríguez-Sánchez, C. Leray, A. Toutant, A. Ferriere, G. Olalde, Development of a new method to estimate the incident solar flux on central receivers from deteriorated heliostats, *Renew. Energy* 130 (2019) 182–190, <https://doi.org/10.1016/j.renene.2018.06.056>.
- [23] M.A. Kant, P. Rudolf Von Rohr, Determination of surface heat flux distributions by using surface temperature measurements and applying inverse techniques, *Int. J. Heat Mass Transf.* 99 (2016) 1–9, <https://doi.org/10.1016/j.ijheatmasstransfer.2016.03.082>.
- [24] J.V. Beck, C. St Clair, B. Blackwell, *Inverse Heat Conduction*, 1985. [http://www.osti.gov/energycitations/product.biblio.jsp?osti\\_id=5792952](http://www.osti.gov/energycitations/product.biblio.jsp?osti_id=5792952).
- [25] A.N. Tikhonov, V.Y. Arsenin, *Solutions of Ill Posed Problems*, 1979.
- [26] K.A. Woodbury, *Inverse Engineering Handbook*, 2003. <http://www.loc.gov/catdir/toc/fy034/2002067743.html>.
- [27] V. Pozzobon, S. Salvador, High heat flux mapping using infrared images processed by inverse methods: an application to solar concentrating systems, *Sol. Energy* 117 (2015) 29–35, <https://doi.org/10.1016/j.solener.2015.04.021>.
- [28] K.S. Reddy, N.P. Singh, S. Somasundharam, In-situ prediction of focal flux distribution for concentrating photovoltaic (CPV) system using inverse heat transfer technique for effective design of receiver, *Sol. Energy* 159 (2018) 510–518, <https://doi.org/10.1016/j.solener.2017.10.079>.
- [29] A. Radwan, S. Ookawara, M. Ahmed, Analysis and simulation of concentrating photovoltaic systems with a microchannel heat sink, *Sol. Energy* 136 (2016) 35–48, <https://doi.org/10.1016/j.solener.2016.06.070>.
- [30] M. Schmitz, N. Wiik, G. Ambrosetti, A. Pedretti, S. Paredes, P. Ruch, B. Michel, A. Steinfeld, A 6-focus high-concentration photovoltaic-thermal dish system, *Sol. Energy* 155 (2017) 445–463, <https://doi.org/10.1016/j.solener.2017.05.087>.
- [31] H. Chen, J. Ji, Y. Wang, W. Sun, G. Pei, Z. Yu, Thermal analysis of a high concentration photovoltaic/thermal system, *Sol. Energy* 107 (2014) 372–379, <https://doi.org/10.1016/j.solener.2014.05.043>.
- [32] Y. Su, Y. Zhang, L. Shu, Experimental study of using phase change material cooling in a solar tracking concentrated photovoltaic-thermal system, *Sol. Energy* 159 (2018) 777–785, <https://doi.org/10.1016/j.solener.2017.11.045>.
- [33] Power from the sun, Chapter 8, (n.d.), <http://www.powerfromthesun.net/Book/chapter08/chapter08.html>. (Accessed 28 December 2018).
- [34] K.S. Reddy, N.P. Singh, S. Somasundharam, In-situ prediction of focal flux distribution for concentrating photovoltaic (CPV) system using inverse heat transfer technique for effective design of receiver, *Sol. Energy* 159 (2018), <https://doi.org/10.1016/j.solener.2017.10.079>.
- [35] M.R. Jones, A. Tezuka, Y. Yamada, Thermal tomographic detection of inhomogeneities, *J. Heat Transf.* 117 (1995) 969, <https://doi.org/10.1115/1.2836318>.
- [36] S. Somasundharam, K.S. Reddy, Simultaneous estimation of thermal properties of orthotropic material with non-intrusive measurement, *Int. J. Heat Mass Transf.* 126 (2018) 1162–1177, <https://doi.org/10.1016/j.ijheatmasstransfer.2018.05.061>.
- [37] Ansys Release, ANSYS mechanical APDL element reference, ANSYS Man. 15317 (2012) 724–746. [www.ansys.com](http://www.ansys.com).
- [38] Thermal Conductivities 2.3.7 (n.d.), [http://www.kayelaby.npl.co.uk/general\\_physics/2\\_3/2\\_3\\_7.html](http://www.kayelaby.npl.co.uk/general_physics/2_3/2_3_7.html). (Accessed 10 December 2018).
- [39] S. Kumar, S.C. Mullick, Wind heat transfer coefficient in solar collectors in outdoor conditions, *Sol. Energy* 84 (2010) 956–963, <https://doi.org/10.1016/j.solener.2010.03.003>.